Preprints.org

Article

Real-time Monitoring of Laser-induced Functionalisation of Transparent Conductive Oxide Films

Takuya Hosokai [*] and Junichi Nomoto

Article

Real-Time Monitoring of Laser-Induced Functionalisation of Transparent Conductive Oxide Films

Takuya Hosokai [1],*, Junichi Nomoto [2]

[1] Research Institute for Material and Chemical Measurement, National Metrology Institute of Japan (NMIJ), National Institute of Advanced Industrial Science and Technology (AIST), Central 5, 1-1-1 Higashi, Tsukuba, Ibaraki 305-8565, Japan

[2] Advanced Manufacturing Research Institute, National Institute of Advanced Industrial Science and Technology (AIST), Central 5, 1-1-1 Higashi, Tsukuba, Ibaraki 305-8565, Japan

* Correspondence: t.hosokai@aist.go.jp

Abstract: Laser-induced functionalisation using excimer laser irradiation has been widely applied to transparent conductive oxide films. However, exploring suitable irradiation conditions is time-consuming and cost-ineffective as there are numerous routine film fabrication and analytical processes. Thus, we herein explored a real-time technique to monitor the laser-induced functionalisation of transparent conductive oxide films. We developed two types of monitoring apparatus, electrical and optical, and applied them to magnetron-sputtered Sn-doped In_2O_3 films grown on glass substrates and hydrogen-doped In_2O_3 films on glass or plastic substrates using a picosecond Nd:YAG pulsed laser. Both techniques could monitor the functionalisation from a change in properties of the films on glass substrates by laser irradiation, but electrical measurement was unsuitable for plastic samples because of a laser-induced degradation of the underlying plastic substrate, which harmed proper electrical contact. Instead, we demonstrated that the optical properties in the near-infrared region were suitable for the monitoring and the changes in the optical properties were visually detected in real-time by using a near-infrared camera.

Keywords: transparent conducting oxide films; laser irradiation; photo-functionalisation; real-time monitoring; Nd:YAG laser

1. Introduction

In_2O_3-based transparent conducting oxide (TCO) films are widely used as transparent electrodes in various opto-electronic devices, such as displays, light-emitting diodes, and solar cells [1-4]. Magnetron-sputtered Sn-doped In_2O_3 (ITO) has been adopted as the TCO material. However, for high-efficiency solar cell applications, solid-phase crystallised hydrogen (H)-doped In_2O_3 (IO:H) and H and transition metals (such as Ce and ICO:H), which exhibit high transparency over a wide range from visible to near-infrared (NIR), have been frequently investigated [5, 6]. However, there is a critical drawback in using flexible substrates, such as polyethylene terephthalate (PET), for these TCO films because of the lowering of the electrical resistivity (ρ); ρ is inversely proportional to the carrier mobility (μ) and carrier concentration (N) [7]. The crystallinity of the TCO films is enhanced by annealing during or post deposition over 150 °C. On PET, the enhancement of μ and/or N by controlling defects and crystallisation is prohibited by the limit of the thermal annealing temperature (less than 150 °C).

To resolve this issue, the excimer laser irradiation (ELI) technique has been used [8-11]. Excimer lasers have a high photon energy. For example, KrF (wavelength λ = 248 nm) excimer lasers can achieve a photon energy of 5 eV, which should be sufficient to induce a photothermal reaction. The temperature inside the film exceeds 400 °C, but only during a very short irradiation time (decay over several hundreds of nanoseconds); therefore, thermal damage to the underlayer can be avoided [10, 11]. Consequently, we obtained a low sheet resistance (R_s) of 14.2 Ω/□ (ρ = 2.13 × 10^{-4} Ωcm) with a

high average optical transmittance in the visible to NIR region, owing to the highest μ of 133 cm²/Vs obtained among reported flexible TCO films [12].

The irradiation conditions of ELI are the repetition rate, power, and the number of shots. To obtain the desired TCO films, suitable laser irradiation conditions must be explored, including the deposition of numerous films and the application of varying laser irradiation conditions to these films. Subsequently, the effects of laser irradiation were verified through various assessments, such as electrical property measurements through Hall effect measurements, X-ray diffraction (XRD), hard X-ray photoemission spectroscopy, and particle analysis using electron microscopies. Such experiments are indispensable for the fabrication of high-performance TCO films; however, these studies incur various costs, such as time, materials, and power. A real-time observation of film properties during laser irradiation should be ideal to reduce the cost of exploring laser irradiation conditions for enhancing or functionalising TCO films through ELI [13].

Several monitoring techniques of the laser-induced crystallization have been developed and applied for semiconducting materials. In early times, Bostangjogo et al. used time-resolved transmission electron microscopy (TEM) and investigated a crystallization process of amorphous silicon (a-Si) and germanium (a-Ge) films in a nanosecond (ns) time scale [14-16]. Nikolova et al. also used time-resolved TEM and characterized the crystallization dynamics of a-Ge films which were supported by Si monoxide membranes [17, 18]. Later, the detail of the dynamics of a-Ge films was unveiled by the same group, which performed a multi-frame dynamic TEM and obtained images of the crystallization from 100 ns [19]. Optical methods are also utilized for monitoring of the laser-induced crystallization. Lee et al. developed a double laser recrystallization system combined with optical microscopy and determined a lateral solidification velocity of a-Si films [20]. Kuo et al. employed optical transmission and reflection spectroscopy and studied phase transitions and exclusive crystallization of a-Si films in ns time scale [21-23]. As the alternative of use of lasers, some investigations to monitor the crystallization of amorphous films during sample heating were conducted by using optical spectroscopies, atomic force microscopy, electrical resistivity measurement method, and in situ XRD [24-33]. Some of the literatures utilized both pulsed lasers and probe lights in visible light region because Si and Ge films can absorb lights in that wavelength region. However, these lasers or lights are hardly applicable or ineffective for TCO films owing to their high transparency in visible region due to their large band gap. On the other hand, the use of excimer laser for development of a real-time monitoring method has other issue. The excimer laser that is needed to crystallize TCO films by light adsorption is challenging to transport to other facilities, e.g., TEM facility or synchrotron beamlines to conduct XRD, owing to its large size [34]. Therefore. to facilitate the exploration of the laser irradiation conditions of TCO films, new development of portable real-time monitoring techniques that are feasible at the laboratory level is desirable.

Accordingly, we propose real-time monitoring techniques to explore the laser irradiation conditions aimed at enhancing the functionality of TCO films. For this development, we employed the fourth-harmonic generation (FHG) of a picosecond Nd:YAG laser instead of excimer laser, owing to limitations in the setup location. The FHG operates at a wavelength of 266 nm (4.66 eV), which is slightly lower in energy than the commonly used excimer laser (5 eV). Although the irradiation energy density of our Nd:YAG laser was lower by a factor of 2.5, compared with the excimer laser used for ELI in our group, laser-induced functionalisation could be expected owing to the much higher peak power of the Nd:YAG laser by a factor of 8.6, as we calculated before experiments. We developed electrical and optical measurement methods. We first introduce the results of the development of the electrical method while noting issues with the electrical measurements. To address the issues identified in the electrical measurement techniques, we also developed optical methods. In this regard, we highlight the effectiveness of observing changes in intensity in the NIR wavelength region derived from variations in carrier concentration, particularly using a NIR camera, as a means of real-time observation of photofunctionalization. The optical method developed in this study, particularly, proves to be effective in cost-effectively exploring laser irradiation conditions for TCO films, as it detects the photofunctionalization in large area and could be adopted to actual manufacturing process.

2. Materials and Methods

The specimens used in this study were radio frequency (RF) (frequency 13.56 MHz) magnetron-sputtered 120-nm-thick ITO films on a quartz glass substrate and ICO:H films on glass or PET substrates. The films were fabricated without intentionally heating the substrates. For these specimens, the FHG of a picosecond diode-pumped solid-state Nd:YAG pulsed laser (PL2211, Ekspla) was used for the photofunctionalisation of the TCO films. The pulse width was ~28 ps, and the beam diameter was ~3 mm (Gaussian beam, $1/e^2$, full width half maximum (FWHM)). The irradiation fluence was 0.43–0.45 mJ/pulse, monitored by a thermal sensor (3A, Ophir).

Two types of real-time monitoring apparatus based on electrical or optical measurements were developed. The method for monitoring the electrical properties is shown in Figure 1. The samples were placed on a ceramic heater and fixed using screws and metal washers from the top films. An electrometer/high-resistance meter (B2987, Keysight) was used for the voltage supply and current measurements, and a thermocouple (TC) data logger (TC-08, Pico Technology) was employed for temperature measurements. Lead wires were used as electrodes. The electrodes were in direct contact with the sample substrate, and the FHG was irradiated between the electrodes. The terminal spacing of the electrodes was set to approximately 4 mm to avoid irradiating the electrodes with FHG. The TC wires were placed between the electrodes but near the centre to avoid direct irradiation of the wires to FHG. It is noted that no adhesives were used for the contact of both electrodes and TC wires with the samples to measure several times on the same sample by changing irradiation spots. FHG, which was transmitted approximately 10% through the ITO samples, was either absorbed or diffusely reflected from the surface of the ceramic heater on the backside of the substrate. The change in resistance after FHG irradiation was measured approximately 10 times at 2.7±0.5 mm between the electrodes using a digital multimeter (CDM-6000, CUSTOM), and the average value was calculated. To identify the effect of FHG irradiation using other measurement methods, raster irradiation of FHG was performed using two motorised transition stages (MTS50-Z8, Thorlabs). Subsequently, Hall effect measurements (Resi Test 8300, TOYO Corporation) and out-of-plane $\theta/2\theta$ XRD measurements (SmartLab XRD System, Rigaku Corp.) were performed.
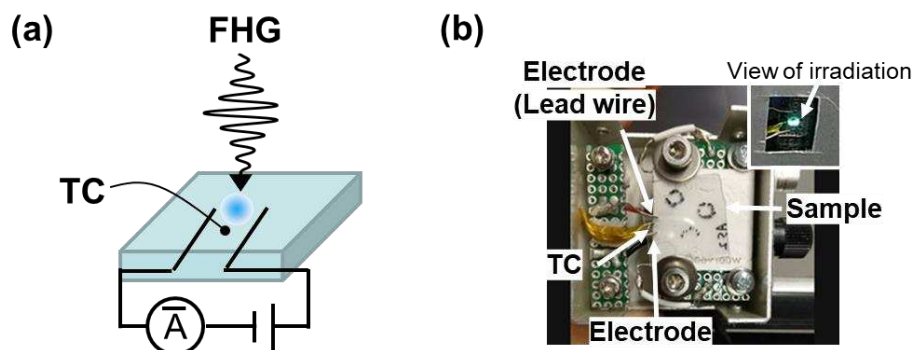

Figure 1. Scheme of electrical measurement setup during FHG irradiation (**a**). Photograph of the measurement conditions (**b**).

Optical properties were monitored using two methods. Figures 2(a) and 2(b) depict the systems employing a mode-locked supercontinuum source (SC) (SC-Pro-M-40 MHz-PP, YSL Photonics) and an LED-ring UV and NIR light, all of which were used as probe lights. To investigate the effect of FHG irradiation, Figure 2(a) shows the changes in the NIR transmittance, whereas Figure 2(b) shows the image changes in the UV and NIR diffuse reflectance using two digital cameras. In Figure 2(a), the SC light is directed onto the sample surface along the normal direction of the substrate without any focus. A parabolic mirror (MPD169-P01, Thorlabs) and a cold mirror (CLDM-50S, Sigma) were used to observe the transmitted light spectra above 700 nm using a photonic multichannel analyser (C10028-01, Hamamatsu). To obtain two-dimensional images, raster irradiation of FHG was performed using motorised transition stages, and the light transmitted through the samples was detected using a biased InGaAs photodiode (DET20C2, Thorlabs) and B2987. For this measurement, the transmitted light was passed through a 1600 nm bandpass filter (BPF). As shown in Figure 2(b), a custom-made ring light alternating between 395 nm LED (LED395L, Thorlabs) and 1600 nm LED (LED1600L, Thorlabs) was directed onto the sample to capture diffuse reflectance images using a

monochrome CMOS camera (CS165MU, Thorlabs) and an InGaAs NIR camera (XS-USB-FPA-1.7-320-TE0-60 Hz-NTSC-VisNIR, Xenics). The diffuse reflectance of UV and NIR light was separated using a cold mirror, and spectral separation was further achieved using 390 nm (FB390-10, Thorlabs) and 1600 nm (65794, Edmund Optics) BPFs. Both cameras were simultaneously operated at 10 fps. The FHG and UV/NIR light transmitted through the sample were blocked using an aluminium protective screen (TPS5, Thorlabs) installed on the backside of the sample.

In all the measurements, the incidence of FHG in the sample was at angles less than 12° from the sample normal. All the measurement programs were developed using LabVIEW software. The measurements were conducted at room temperature (296 K).
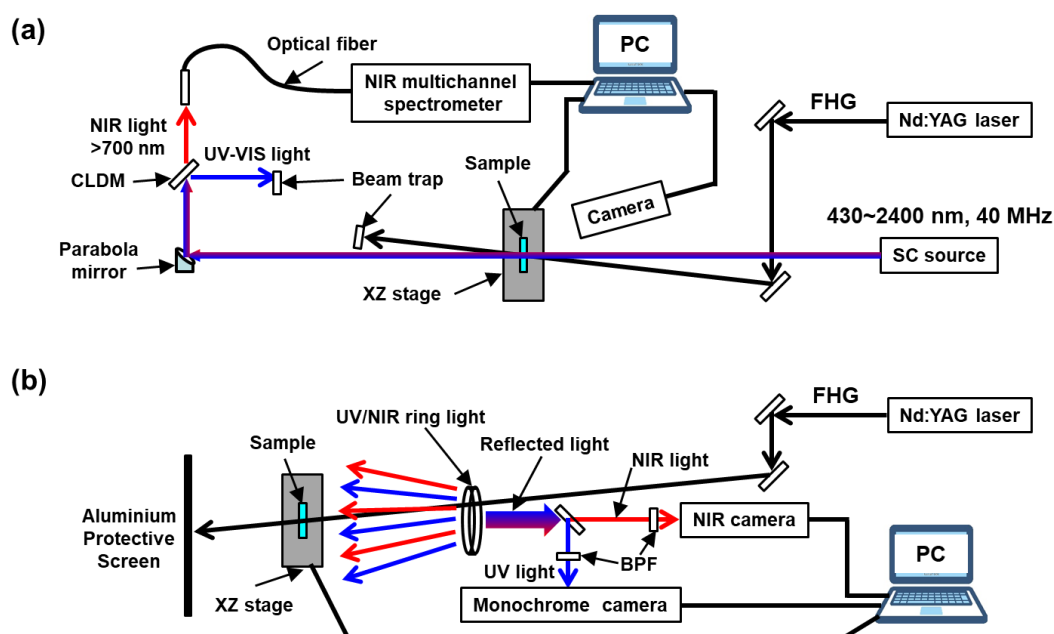

Figure 2. Scheme of the two types of optical measurement setups: (a) spectroscopic and single-point scanning measurement setup and (**a**) light reflectance image monitoring setup with two cameras (**b**).

3. Results and Discussion

3.1. Electrical Monitoring System: Contact Method

3.1.1. ITO/quartz Glass

First, we investigated the effect of FHG irradiation on the electrical properties of ITO films. Figures 3(a) and 3(b) show the temporal results of temperature and current of an ITO film grown on a quartz glass substrate by FHG irradiation under a bias voltage of 0.5 V. Under irradiation, both the temperature and current increased immediately, and the temperature rose to 51 °C from an initial value of 26 °C. After the irradiation was stopped, the temperature decreased steeply and returned to the initial temperature. This result was reproducible after a second irradiation. On the other hand, the current also increased but the rate of increase was lower than that of the temperature. Such slow behaviour was also observed after stopping the irradiation; the current at high temperatures remained constant for ~300 s and dropped to a value slightly larger than the initial base current. A larger base current was also observed after the second irradiation. It is supposed that the resistance of the ITO films was reduced by the FHG irradiation. However, a large drift in the base current was observed after the two irradiations. For instance, the base current after the 1st irradiation increased by 2.5% and further increased by 1.0% owing to the drift. Thus, long-term irradiation can enable a change in the electrical properties of the ITO film but may not be suitable to assess rigorously the improvement in the properties by the present contact method. The large drift might be caused by the latent heat of the sample system owing to laser absorption.

To clarify the effect of FHG irradiation, short-term irradiation with FHG pulses was conducted on a fresh spot of the ITO film. Irradiation for 5 s was repeated five times on the same spot. The temporal results of the temperature and current are shown in Figures 3(c) and 3(d), respectively. The

temperature increased transiently by only approximately 3 °C under each irradiation, showing that the short-time irradiation largely suppressed the increase in the temperature. For the irradiation processes, the current also transiently increased by 3%–5% from the initial current and had no delay with respect to the temperature, which differed from the long-term irradiation condition (Figures 3(a) and 3(b)). Remarkably, the base current after the final irradiation maintained a larger value of ~3% compared with the initial value, and no drift to a larger current was confirmed. These results suggest that the resistance of the ITO film decreased upon FHG irradiation. The resistance of the sample across the irradiated spot was measured 20 times using the two-terminal method with a multimeter. The averaged resistance and standard deviation were evaluated to be 275 ± 36 Ω, which was significantly lower than that before the irradiation, that is, 325 ± 24 Ω. It is clear that the resistance of the ITO sample was reduced by FHG irradiation.
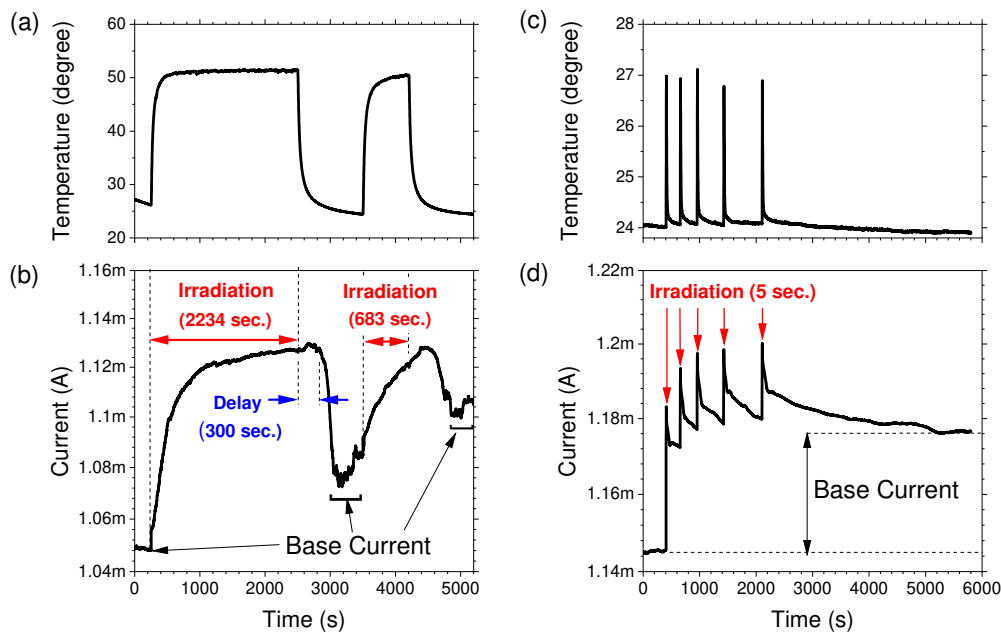

Figure 3. Temporal results of the temperature (top) and current (bottom) of the ITO film under FHG irradiation. (**a**) and (**b**) show the results for long-time irradiation. (**c**) and (**d**) show the results for short-time irradiation.

The improvement in the electric properties of the ITO films by FHG irradiation was investigated quantitatively by Hall effect measurements and out-of-plane XRD. For these measurements, the FHG was irradiated on a large area (8 × 17 mm²) of another ITO film on quartz glass by scanning the irradiation; the sample was moved 1 mm at a time and irradiated for 25 s at each spot. The effect of irradiation is shown in Figure 4(a), where the area shows a lamellar texture that becomes more transparent. The resistance was 132 ± 20 Ω in the irradiated area, whereas that in the non-irradiated area was 275 ± 12 Ω. The results of the Hall effect measurements are summarised in Table 1. The electrical resistivity was improved from 5.25×10^{-4} Ω/cm to 2.73×10^{-4} Ω/cm, confirming the improvement in the electrical property of the ITO film by FHG irradiation, similar to ELI [35].
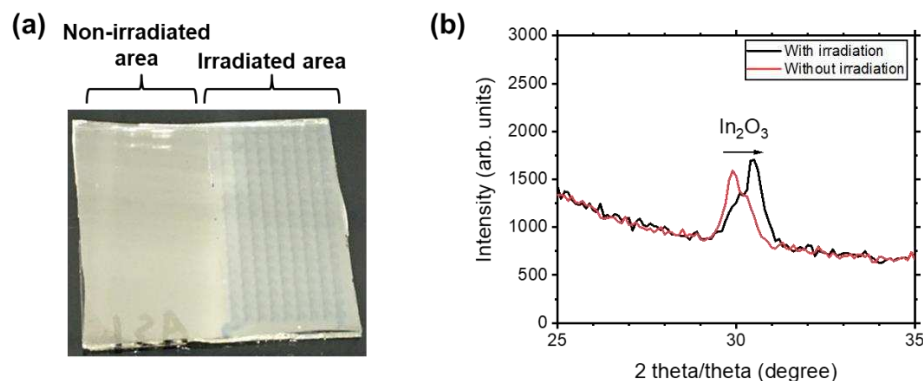
Figure 4. FHG irradiation effect on the ITO film (**a**). Out-of-plane XRD results before and after the FHG irradiation (**b**).

An analysis of the results of the Hall effect measurement (Table 1) revealed that the improvement in the electrical resistance of the ITO films was caused by an increase in the carrier concentration by a factor of two and not by Hall mobility. The out-of-plane XRD patterns in Figure 4(b) show a slight enhancement in the crystallisation of the ITO film. The as-deposited ITO films exhibited 222 diffraction peaks corresponding to a cubic In_2O_3 bixbyite structure, which seemed to split into two peaks at 29.8° and 30.1°. The splitting into two peaks is attributed to the difference in crystallisation between the vapour and solid phases produced by the deposition process [36]. After FHG irradiation, the intensity of the lower-diffraction-angle reflection decreased, whereas that of the higher-diffraction-angle reflection increased. This indicates the FHG-derived acceleration of film crystallisation. However, for the more crystalline ITO films, no change in Hall mobility was observed after irradiation (see Table 1). The FHG irradiation activated the Sn dopants by the dissociation of the interstitial oxygen, which formed a neutral cluster with Sn, thus increasing the number of charge carriers [35, 37, 38]. The decrease in defects is attributed to the transparent optical property of the irradiated area in Figure 4(a), as decreasing of the defect states in the band gap of the ITO films within the visible light region is also occured. The carrier concentration increased to an order of magnitude of 21, which suggests that ionised impurity scattering by the Sn dopants also significantly affected the Hall mobility [39]. Thus, the hypothetical increase in Hall mobility owing to crystallisation was compensated by the ionised impurity scattering caused by the increase in carrier concentration.

Table 1. Electrical properties of the ITO films obtained by Hall effect measurements.

Sample area	Resistivity (Ωcm)	Carrier concentration (cm^{-3})	Hall mobility (cm^2/V s)
Non-irradiated	5.25×10^{-4}	5.48×10^{20}	21.3
Irradiated	2.73×10^{-4}	1.09×10^{21}	20.9

Finally, we tested the effect of the laser repetition rate on the electrical properties of the ITO films. The ITO films were irradiated with FHG pulses at the four different repetition rates of 1 Hz, 10 Hz, 100 Hz, and 1 kHz while maintaining the total number of irradiated pulses at 20000. The results are summarised in Table 2. Upon decreasing the rate, the degree of temperature increase (ΔT) was reduced significantly. As the repetition rate was decreased from 1 kHz to 100 Hz, ΔT became less than 1 °C, and at 1 Hz, no ΔT was detected. Inspite of the different ΔTs, resistance decreased to nearly the same value in all the conditions. These results indicate that the improvement in the electrical properties occurred owing to one pulse irradiation event and the degree of the improvement is depended on the number of pulses. While it is known that the electrical properties of ITO films are improved by heating at 200 °C, our result suggests that the photochemical reaction by FHG can contribute to the improvement, which is known for ELI [35].

Table 2. Repetition rate dependence on the resistance and temperature increase of ITO films.

Repetition rate (Hz)	Resistance (Ω)		ΔT (°C)
	Before irradiation	After irradiation	
1	184	167	Not detectable
10	181	168	~0.01
100	182	163	0.3
1000	181	166	37.7

3.1.2. ICO:H/PET Films

Subsequently, we employed the established electrical monitoring technique for the ICO:H films grown on PET films, which are candidates for flexible electrodes. However, when starting the irradiation, damage to the specimens was easily observed. Figure 5(a) shows the photographs of the specimens as a function of the number of irradiated pulses. Whereas 100 and 1000 pulses exhibited no change, 2000 pulses induced a circle-like deformation. Furthermore, the deformation increased as

the number of pulses increased. At the same laser power condition, we tested the effect on current measurements and observed poor reproducibility; the current either increased or decreased (see the Supplementary Materials section).

As the current was measured by direct contact with the lead wires on the samples, poor reproducibility was considered to be caused by the deformation of the plastic substrate. Such deformations of the ICO:H/PET films have been reported for ELI [39]. The excimer laser had a thermal effect on the plastic films, and the deformation of the PET films broke the top layer of the ICO:H films. Such deformation was avoided by inserting a SiO_2 buffer layer between the ICO:H and PET films, and the electrical properties of the ICO:H/PET film were improved [40]. For the ICO:H/SiO_2/PET samples, we conducted FHG irradiation and monitored the current (Figure 5(b)). We obtained an increase in the base current by 7.7% after irradiation for 194 s. However, as shown in Figure 5(b), the current suddenly increased transiently when irradiation was stopped. This was not the case for the ITO/quartz glass samples (Figure 3(b)). It can be assumed that, during FHG irradiation, the PET films of the ICO:H/SiO_2/PET samples were also slightly deformed, and unstable electrical contact was induced. In conclusion, electric monitoring by direct contact can be adopted for glass substrates that have high durability for laser irradiation, but is not suitable for PET substrates owing to the issue of electrical contact.
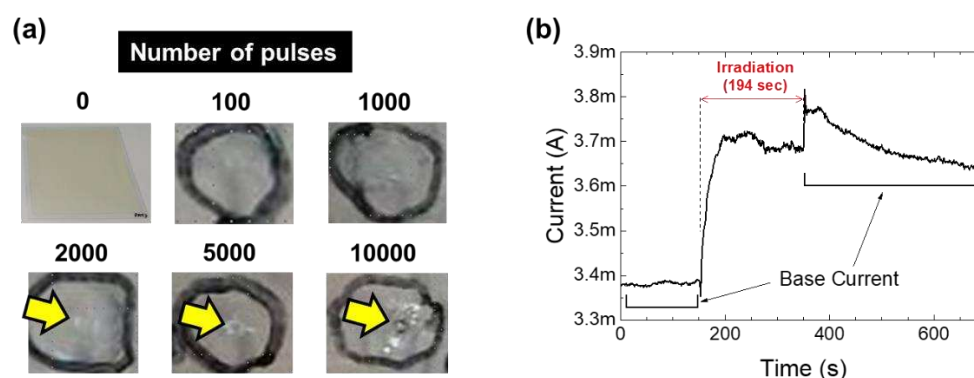

Figure 5. Image of a series of FHG pulses irradiated onto the ICO:H/PET film (**a**). The "0" picture is a full picture of the sample, and the others are enlarged ones. FHG was irradiated inside the black circles. Temporal result of the current of the ICO:H/SiO_2/PET film under FHG irradiation (**b**).

3.2. Optical Monitoring System: Non-contact Method

3.2.1. Single-point Measurement System

The transmission spectrum of the ICO:H/glass substrate is shown in Figure 6(a). The ICO:H film exhibited a sharper change in the transmission peak at around 394 nm, which corresponds to a bandgap of the film, owing to laser-induced crystallisation, and the transmittance in the NIR region above 1000 nm increased by approximately 10% over longer wavelengths. Figure 6(b) illustrates the time-dependent change in the relative transmission intensity (ΔI) of SC light at a wavelength of 1600 nm before and after FHG irradiation. Here, ΔI is defined as $\Delta I = (I_0 - I) / I_0 * 100$ [%], where I_0 represents the average intensity before the irradiation. Despite the relatively significant noise of approximately ±1% arising from the stability of the SC light source, the rapid change in ΔI owing to FHG irradiation appeared exponentially, resulting in an average increase of approximately 7.7% (refer to the simulation curve in Figure 6(b)). Upon ceasing FHG irradiation, although ΔI momentarily decreased, it remained 4.5% greater than that before irradiation. As such ΔI changes were not observed with the substrate alone, it can be concluded that the observed ΔI after the FHG irradiation was due to a change in the optical property of the ICO:H film.
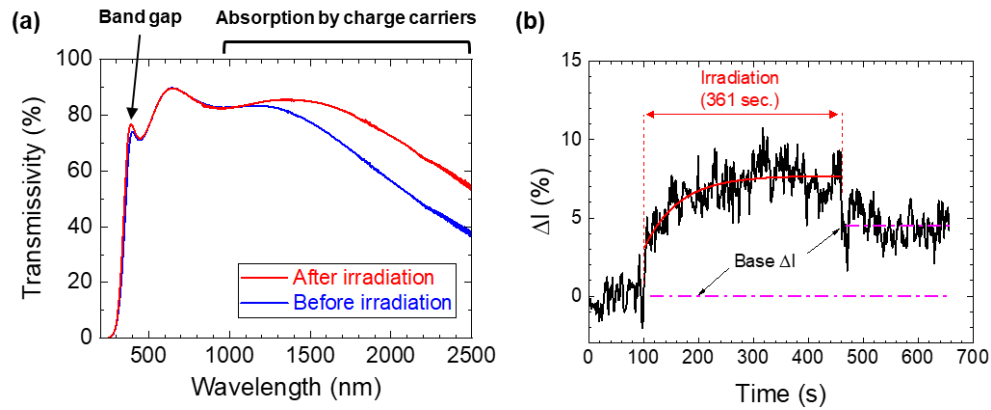
Figure 6. Transmission spectra of the ICO:H/glass system: before (blue) and after (red) ELI (**a**). Temporal results of ΔI of the ICO:H/glass system by FHG irradiation (**b**). The red curve in (**b**) is a simulation curve using an exponential decay function.

Next the transmitted SC light intensity at a wavelength of 1650 nm through the ICO:H/glass was detected as an two-dimensional (2D) image using the InGaAs detector. Figures 7(a) and 7(b) show photographs of two samples: a bare glass substrate and ICO:H/glass. These samples were scanned two-dimensionally using motors, and the 2D maps of the transmitted intensity are shown in Figures 7(c) and 7(d). In the case of the bare substrate (Figure 7(c)), the areas around the substrate, that is, the air region, exhibited an intense red colour. Based on the intensity in the air region, the transmittance in the substrate area, displayed in orange, was calculated to be 94%. For the ICO:H/glass sample, the transmittance decreased further, as shown in Figure 7(d), to approximately 70%, which is similar to the transmittance shown in Figure 6(a) before laser irradiation. For this sample, FHG was irradiated along the Z-axis direction for only one scan, and a magnified view of the transmittance 2D image is shown in Figure 7(e). The colour near the X-axis of the FHG irradiation at approximately 2 mm shifted towards warmer tones in the Z-axis direction, indicating an increase in transmittance. The results for the range of Z = 13–14 mm in Figure 7(e), extracted in the X-axis direction, are shown in Figure 7(f). The spectrum is observed as a Gaussian function centred at approximately 2 mm. By employing Gaussian curve-fitting on the result, the FWHM of the region where the intensity increased was observed to be 0.55 mm, and the range determined from the threshold of the Gaussian curve was 1.11 mm. Given that the beam diameter of FHG was φ 3 mm (1/e², FWHM), it can be concluded that the property change in the ICO:H film owing to FHG irradiation did not occur across the entire FHG beam diameter; only the limited area around the laser peak spot could be crystallized. The energy threshold for the property changes of the ICO:H film induced by FHG irradiation, calculated from the above beam diameter and simulated 2D Gaussian curve, was 0.12 μJ.

Subsequently, a line scan of FHG irradiation was performed at intervals of 0.5 mm, and repeated four times. The resulting images of the intensity changes and transmittance spectra are shown in Figures 7(g) and 7(h), respectively. By expanding the irradiation area in Figures 7(e) and 7(f), an increase in transmittance was observed over a wider area. The most significant transmittance change occurred in the region spanning ±5 mm of the Z-direction from the centre of the substrate, with a value of 8.1%. This value closely aligns with the 10% transmittance change observed before and after ELI, as shown in Figure 6(a). This demonstrates that the optical property changes caused by FHG irradiation are comparable to those caused by ELI.
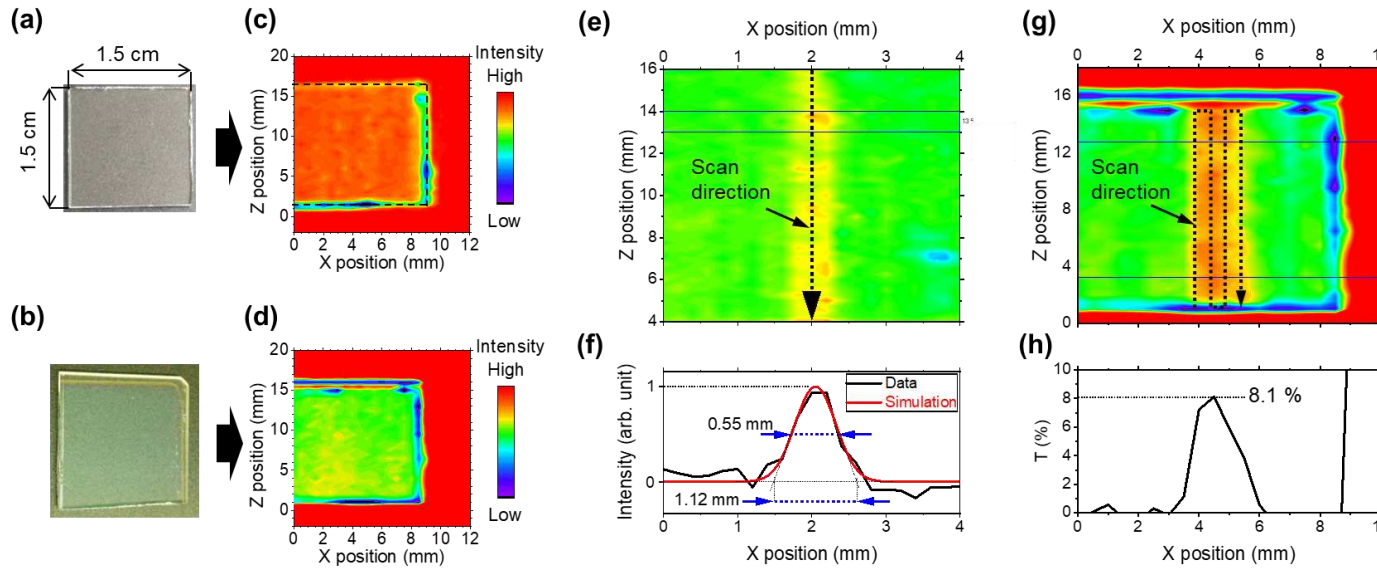
9

Figure 7. Photo and 2D image of transmission intensity at a wavelength of 1650 nm for SC light: bare glass substrate ((**a**) and (**c**)) and ICO:H/glass sample ((**b**) and (**d**)). 2D image after one line scan of the FHG irradiation (**e**) and its intensity profile (**f**). 2D image after four line scans of the FHG irradiation (**g**) and its transmittance profile (**h**).

3.2.2. UV/NIR Camera System

The previous subsection demonstrated the visualisation of optical property changes in the ICO:H films by FHG irradiation using a single photodetector. However, this method is time-consuming, because it requires multiple movements of the sample to acquire images. Scaling up to larger areas for observation is also challenging, and accurately aligning the FHG and SC light sources at the same spot on the sample surface is not straightforward.

To address these limitations, a real-time imaging system was constructed to observe the optical property changes in the ICO:H films induced by FHG irradiation using UV (395 nm) and NIR (1600 nm) LEDs as light sources and two cameras as detectors, as shown in Figure 2(b). To test the system, we used an ICO:H/glass sample that was initially irradiated with FHG under conditions programmed for the XZ stages, as illustrated in Figure 8(a), with a rat-shaped configuration, which was confirmed by acquiring an image of the transmittance using SC light (Figure 8(d)), as explained in Subsection 3.2.1. Using this sample, we present the UV and NIR images of the ICO:H/glass system captured by the developed camera system in Figures 8(c) and 8(d), respectively. The 3 cm square sample substrate was affixed to the XZ stage using a metal plate. Both the UV image (Figure 8(c)) and NIR image (Figure 8(d)) depict the rat-shaped pattern observed in Figure 8(b). The NIR image exhibited a sharper contrast for the pattern than the UV image. This difference was consistent with the transmittance changes before and after laser irradiation in the UV and IR regions, as shown in Figure 6(a).
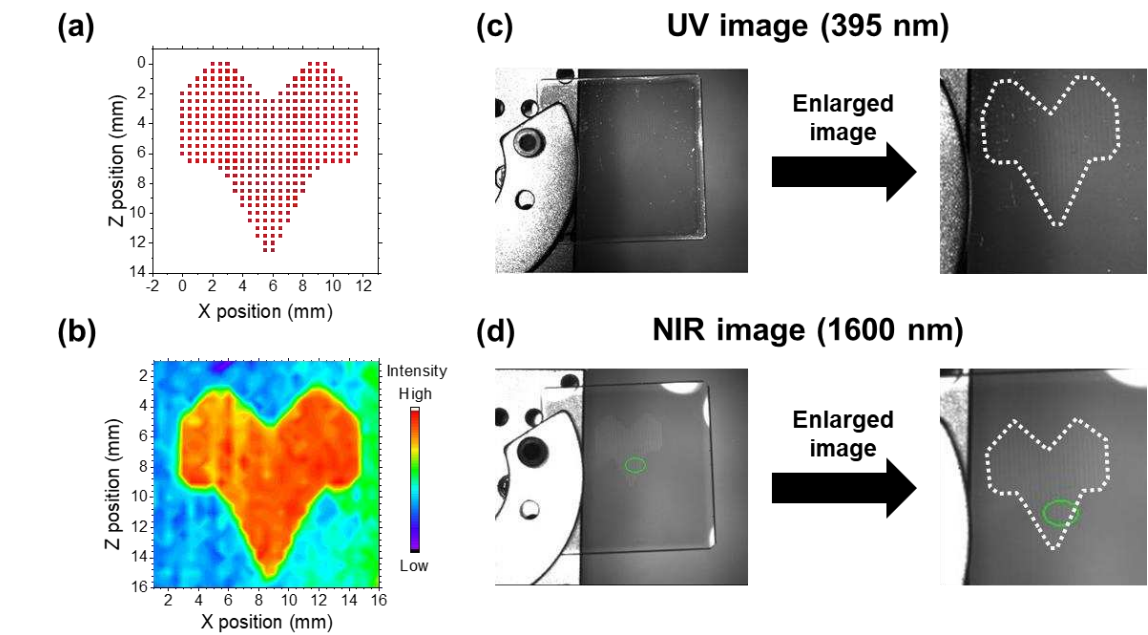
Figure 8. Simulation of FHG irradiation (**a**) and its result for ICO:H/glass (**b**) for an SC light source. UV (**c**) and NIR (**d**) images of the sample with the irradiated pattern in (**b**). The left and right images are full pictures and enlarged images of the irradiated position (blue broken pattern), respectively. For this system, intensity accumulated in a given region—for instance, the green circle region in (d)—can be monitored in real time.

After confirming the distinguishability of light transmittance changes in the ICO:H films induced by FHG irradiation through UV and NIR images, we performed real-time imaging measurements of these variations. Figure 9 shows the temporal UV and NIR images captured during the FHG irradiation of the ICO:H/glass sample (the movie is shown in the Supplementary Materials). Under the FHG irradiation, the profile of the laser light was observed in the UV image, whereas it was absent in the NIR image. When the sample was moved using the XZ stage to trace a square pattern with laser light, the contrast in the NIR image decreased linearly, whereas in the UV image, the FHG light was too intense and impeded the observation of contrast changes. The contrast variations observed in the NIR images are distinctly visible in the differential images. Although the changes in the properties of the ICO:H film induced by laser light were not discernible in the UV images, they were observable in the NIR images.
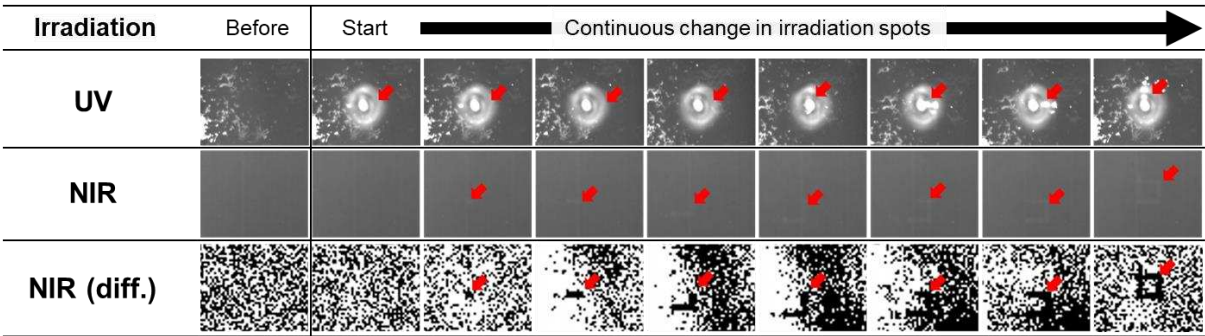

Figure 9. Temporal UV and NIR images of FHG irradiation on the ICO:H/glass samples. The images are selected from a movie shown in Supplementary Materials. The bottom images are differentials of the NIR images.

4. Conclusions

This study was dedicated to the development of real-time monitoring methodologies for the functionalisation of TCO films using laser light irradiation. Monitoring techniques have the potential to yield significant advantages, not only in terms of reducing the temporal expenses associated with

identifying optimal irradiation conditions but also in facilitating a comprehensive exploration of the underlying mechanisms governing functionalisation phenomena. In this study, an electrical measurement system was devised to track alterations in the electrical properties of ITO/glass samples induced by FHG irradiation effectively. The observed enhancement in resistance was substantiated by Hall effect measurements and XRD analysis. Nonetheless, the sensitivity of this technique to electrode contact renders it less suitable for application to plastic substrates. The deformation caused by the FHG irradiation of the substrate introduces instability in the context of constant-current measurements.

To address these limitations, alternative optical methodologies capable of non-distractive and remote detection of changes in the physical characteristics of TCO films have been proposed. Notably, we have shown the efficacy of an NIR imaging technique enabled by an NIR camera in capturing real-time changes in photophysical properties induced by FHG irradiation. The viability of this technique has been proven. However, the application of a UV camera is hindered by the intense FHG beam, which obscures the irradiated spot within the image. Collectively, the results of these investigations support the proposition of a non-contact and non-destructive monitoring approach employing an NIR camera. This approach holds promise for the application of monitoring strategies in the laser-induced functionalisation of TCO films on a larger scale. These contributions have the potential to advance the research in this domain significantly.

References

1. Granqvist, C. G.; Hultåker, A. Transparent and conducting ITO films: new developments and applications. *Thin Solid Films* **2002**, *411*, 1–5.
2. Porch, A.; Morgan, D. V.; Perks, R. M.; Jones, M. O.; Edwards, P. P. Electromagnetic absorption in transparent conducting films. *J. Appl. Phys.* **2004**, *95*, 4734–4737.
3. Calnan, S.; Tiwari, A. N. High mobility transparent conducting oxides for thin film solar cells. *Thin Solid Films* **2010**, *518*, 1839–1849.
4. Klein, A. Transparent conducting oxides: electronic structure–property relationship from photoelectron spectroscopy with *in situ* sample preparation. *J. Am. Ceram. Soc.* **2013**, *96*, 331–345.
5. Koida, T.; Fujiwara, H.; Kondo, M. Reduction of optical loss in hydrogenated amorphous silicon/crystalline silicon heterojunction solar cells by high mobility hydrogen-doped In_2O_3 transparent conductive oxide. *Appl. Phys. Express* **2008**, *1*, 041501.
6. Koida, T.; Ueno, Y.; Shibata, H. In_2O_3-based transparent conducting oxide films with high electron mobility fabricated at low process temperatures. *Phys. Status Solidi A* **2018**, *215*, 1700506.
7. Dixon, S. C.; Scanlon, D. O.; Carmalt, C. J.; Parkin, I. P. n-Type doped transparent conducting binary oxides: an overview. *J. Mater. Chem. C* **2016**, *4*, 6946–6961.
8. Hosono, H.; Kurita, M.; Kawazoe, H. Excimer laser crystallization of amorphous indium-tin-oxide and its application to fine patterning. *Jpn. J. Appl. Phys.* **1998**, *37*, L1119–L1121.
9. Tsuchiya, T.; Niino, H.; Yabe, A.; Yamaguchi, I.; Manabe, T.; Kumagai, T.; Mizuta, S. Characterization of tin-doped indium oxide films prepared by coating photolysis process. *Appl. Surf. Sci.* **2002**, *197-198*, 512–515.
10. Nakajima, T.; Tsuchiya, T.; Ichihara, M.; Nagai, H.; Kumagai, T. Epitaxial growth mechanism for perovskite oxide thin films under pulsed laser irradiation in chemical solution deposition process. *Chem. Mater.* **2008**, *20*, 7344–7351.

11. Nakajima, T.; Shinoda, K.; Tsuchiya, T. A universal value of effective annealing time for rapid oxide nucleation and growth under pulsed ultraviolet laser irradiation. *Phys. Chem. Chem. Phys.* **2013**, *15*, 14384–14389.

12. Nomoto, J.; Koida, T.; Yamaguchi, I.; Makino, H.; Kitanaka, Y.; Nakajima. T.; Tsuchiya, T. Over 130 cm2/Vs Hall mobility of flexible transparent conductive In2O3 films by excimer-laser solid-phase crystallization. *NPG Asia Materials* **2022**, *14*, 76.

13. Ping-Han Wu.; Chih-Lin Huc.; Shih-Wei Feng.; Hong-Tsu Young.; Ming-Yen Lu.; Hsiang-Chen Wang. Real time monitoring of fs laser annealing on indium tin oxide. *Optics and Laser Technology* **2019**, *111*, 380–386.

14. Bostanjoglo, O. Time-resolved TEM of pulsed crystallization of amorphous Si and Ge films. *Phys. Status Solidi A* **1982**, *70*, 473–481.

15. Bostanjoglo, O.; Endruschat, E. Kinetics of Laser-Induced Crystallization of Amorphous Germanium Films, *Phys. Status Solidi A* **1985**, *91*, 17–28.

16. Bostanjoglo, O.; Marine, W.; Thomsen-Schmidt, P. Laser-induced nucleation of crystals in amorphous Ge films. *Appl. Surf. Sci.* **1992**, *54*, 302–307.

17. Nikolova, L.; LaGrange, T.; Reed, B. W.; Stern, M. J.; Browning, N. D.; Campbell, G. H.; Kieffer, J.-C.; Siwick, B. J.; Rosei, F. Nanocrystallization of amorphous germanium films observed with nanosecond temporal resolution. *App. Phys. Lett.* **2010**, 97, 203102.

18. Nikolova, L.; LaGrange, T.; Stern, M. J.; MacLeod, J. M.; Reed, B. W.; Ibrahim, H.; Campbell, G. H.; Rosei, F.; Siwick, B. J. Complex crystallization dynamics in amorphous germanium observed with dynamic transmission electron microscopy. *Phys. Rev. B* **2013**, 87, 064105.

19. Santala, M. K.; Raoux, S.; Campbell, G. H. Kinetics of liquid-mediated crystallization of amorphous Ge from multi-frame dynamic transmission electron microscopy. *Appl. Phys. Lett.* **2015**, *107*, 252106.

20. Lee, M.; Moon, S.; Grigoropoulos, C. P. In situ visualization of interface dynamics during the double laser recrystallization of amorphous silicon thin films. *J. Cryst. Growth* **2001**, *226*, 8–12.

21. Kuo, C.-C.; Yeh, W.-C.; Lee, J.-F.; Jeng, J.-Y. In-Situ and Ex-Situ Measurements on Silicon Thin Films Fabricated by Excimer Laser Annealing. *J. Phys.: Conf. Ser.* **2006**, *48*, 937.

22. Kuo, C.-C.; Yeh, W.-C.; Chen, J.-B.; Jeng, J.-Y. Monitoring explosive crystallization phenomenon of amorphous silicon thin films during short pulse duration XeF excimer laser annealing using real-time optical diagnostic measurements. *Thin Solid Films* **2006**, *515*, 1651–1657.

23. Kuo, C.-C.; Yeh, W.-C.; Lee, J.-F.; Jeng, J.-Y. Effects of Si film thickness and substrate temperature on melt duration observed in excimer laser-induced crystallization of amorphous Si thin films using in-situ transient reflectivity measurements. *Thin Solid Films* **2007**, *515*, 8094–8100.

24. Nguyen, H. V.; An, I.; Collins, R. W. Evolution of the optical functions of thin-film aluminum: A real-time spectroscopic ellipsometry study. *Phys. Rev. B* **1993**, *47*, 3947.

25. Pearce, R.; Vancso, G. J. Real-time imaging of melting and crystallization in poly(ethylene oxide) by atomic force microscopy. *Polymer* **1998**, *39*, 1237–1242.

26. Ow-Yang, C. W.; Spinner, D.; Shigesato, Y.; Paine, D. C. A time-resolved reflectivity study of the amorphous-to-crystalline transformation kinetics in dc-magnetron sputtered indium tin oxide. *J. Appl. Phys.* **1998**, *83*, 145–154.

27. Morikawa, H.; Fujita, M. Crystallization and decrease in resistivity on heat treatment of amorphous indium tin oxide thin films prepared by d.c. magnetron sputtering. *Thin Solid Films* **1999**, *339*, 309-313.

28. Adurodija, F. O.; Semple, L.; Brüning, R. Real-time in situ crystallization and electrical properties of pulsed laser deposited indium oxide thin films. *Thin Solid Films* **2005**, *492*, 153–157.

29. Adurodija, F. O.; Semple, L.; Brüning, R. Crystallization process and electro-optical properties of In2O3 and ITO thin films. *J. Mater. Sci.* **2006**, *41*, 7096–7102.

30. Kim, D.-H.; Hong, W.-E.; Ro, J.-S.; Lee, S. H.; Lee, C.-H.; Park, S. In-situ observation of phase transformation in amorphous silicon during Joule-heating induced crystallization process. *Thin Solid Films* **2011**, *519*, 5516–5522.

31. Rogozin, A.; Vinnichenko, M.; Shevchenko, N.; Kreissig, U.; Kolitsch, A.; Möller, W. Real-time evolution of electrical properties and structure of indium oxide and indium tin oxide during crystallization. *Scr. Mater.* **2009**, *60*, 199-202.

32. Furubayashi, Y.; Kobayashi, S.; Maehara, M.; Ishikawa, K.; Inaba, K.; Sakemi, T.; Kitami, H.; Yamamoto, T. Evolution of implicate order from amorphous to polycrystalline Sn-doped In2O3 films determined by in situ two-dimensional X-ray diffraction measurements. *Appl. Phys. Express* **2020**, *13*, 065502.

33. Jia, J.; Iwasaki, S.; Yamamoto, S.; Nakamura, S.; Magome, E.; Okajima, T.; Shigesato, Y. Temporal Evolution of Microscopic Structure and Functionality during Crystallization of Amorphous Indium-Based Oxide Films. *ACS Appl. Mater. Interfaces* **2021**, *13*, 31825–31834.

34. Hosokai, T.; Gerlach, A.; Hinderhofer, A.; Frank, C.; Ligorio, G.; Heinemeyer, U.; Vorobiev, A.; Schreiber, F. Simultaneous in situ measurements of x-ray reflectivity and optical spectroscopy during organic semiconductor thin film growth. *Appl. Phys. Lett.* **2010**, *97*, 063301.

35. Nomoto, J.; Matsui, H.; Yamaguchi, I.; Nakajima, T.; Tsuchiya, T. Origin of simultaneous enhancement of work function and carrier concentration in In_2O_3 films by excimer-laser irradiation. *Appl. Phys. Lett.* **2021**, *118*, 101602.

36. Yi, C. H.; Shigesato, Y.; Yasui, I.; Takaki, S. Microstructure of Low-Resistivity Tin-Doped In-dium Oxide Films Deposited at 150~200°C, *Jpn. J. Appl. Phys.* **1995**, *34*, L244–L247.

37. Frank, G.; Köstlin, H. Electrical properties and defect model of tin-doped indium oxide layers. *Appl. Phys. A* **1982**, *27*, 197–206.

38. Gonzalez, G. B.; Cohen, J. B.; Hwang, J.-H.; Mason, T. O.; Hodges, J. P.; Jorgensen, J. D. Neutron diffraction study on the defect structure of indium–tin–oxide. *J. Appl. Phys.* **2001**, *89*, 2550–2555.

39. Yamada, N.; Yasui, I.; Shigesato, Y.; Li, H.; Ujihira, Y.; Nomura, K. Donor Compensation and Carrier-Transport Mechanisms in Tin-doped In_2O_3 Films Studied by Means of Conversion Electron ^{119}Sn Mössbauer Spectroscopy and Hall Effect Measurements. *Jpn. J. Appl. Phys.* **2000**, *39*, 4158–4163.

40. Nomoto, J.; Yamaguchi, I.; Nakajima, T.; Matsubayashi, Y.; Tsuchiya, T. Excimer laser annealing method for achieving low electrical resistivity and high work function in transparent conductive amorphous In_2O_3:Zn films on a polyethylene terephthalate substrate. *Thin Solid Films* **2020**, *698*, 137867.